Kinetic Prediction of Reverse Intersystem Crossing in Organic Donor–Acceptor Molecules

Naoya Aizawa,[1,2]* Yu Harabuchi,[2,3,4]* Satoshi Maeda[3,4] and Yong-Jin Pu[1]

[1] RIKEN Center for Emergent Matter Science (CEMS), 2-1 Hirosawa, Wako, Saitama, 351-0198, Japan.

[2] Precursory Research for Embryonic Science and Technology (PRESTO), Japan Science and Technology Agency (JST), 4-1-8 Honcho, Kawaguchi, Saitama 332-0012, Japan.

[3] Department of Chemistry, Faculty of Science, Hokkaido University, Kita 10, Nishi 8, Kita-ku, Sapporo 060-0810, Japan.

[4] Institute for Chemical Reaction Design and Discovery (WPI-ICReDD), Hokkaido University, Kita 21 Nishi 10, Kita-ku, Sapporo, Hokkaido 001-0021, Japan.

Corresponding Authors: E-mail: naoya.aizawa@riken.jp (N.A.); y_harabuchi@sci.hokudai.ac.jp (Y.H.)

Abstract

Reverse intersystem crossing (RISC), the uphill spin-flip process from triplet to singlet excited states, plays a key role in a wide range of photochemical applications. Understanding and predicting the kinetics of such process in vastly different molecular structures would best lead to rational design of new materials. Here, we demonstrate a theoretical expression that successfully reproduces experimental RISC rate constants ranging over five orders of magnitude in twenty different molecules. We show that the spin flip occurs across the singlet–triplet crossing seam involving a higher-lying triplet excited state, where the semi-classical Marcus parabola is no longer valid. The present model explains counterintuitive substitution effects of bromine on the RISC rate constants in newly synthesized molecules, proving as predictive tool for materials design.

Introduction

Electronic spin-flip processes in molecular excited states have gained increasing interest for optoelectronics[1-3], photocatalytic synthesis[4-6] and biomedical applications[7-9]. A relevant example is reverse intersystem crossing (RISC), the uphill transition of a non-emissive triplet excited state to emissive singlet excited state. Such process leads to E-type delayed fluorescence, also known as thermally activated delayed fluorescence (TADF), and allows an internal charge-to-photon conversion efficiency of nearly 100% in organic light-emitting diodes[10]. Although new materials have typically discovered experimentally, fundamental understanding and prediction of RISC kinetics may open vast opportunities for theory-driven materials discovery.

RISC kinetics is often understood in the framework of the Marcus theory[11-14]. If the spin–orbit coupling H_{SO} between the initial triplet and final singlet excited states is weak so that the spin flip only occurs on the crossing seam between their potential energy surfaces (PESs) (Fig. 1a), the RISC rate constant (k_{RISC}) follows a Marcus-like non-adiabatic expression:

$$k_{RISC} = \frac{2\pi}{\hbar}\left|H_{SO}\right|^2 \left(4\pi\lambda k_B T\right)^{-\frac{1}{2}} \exp\left(\frac{-E_A}{k_B T}\right) \quad (1)$$

with $\hbar$ the reduced Planck constant, k_B the Boltzmann constant, T the temperature, λ the reorganization energy and E_A the activation energy to reach the crossing seam. In the case of simple parabolic PESs with equal force constants, which is one crucial assumption of the Marcus theory, E_A can be analytically expressed as

$$E_A = \frac{\left(\Delta E_{ST} + \lambda\right)^2}{4\lambda} \quad (2)$$

with ΔE_{ST} the adiabatic singlet–triplet energy difference. A key implication of Equation (1) and (2) is that k_{RISC} can be predicted from the equilibrium geometries, which correspond to the easily computable local minima on the PESs of the initial triplet state and final singlet state. However, this picture of RISC becomes more complicated if the spin-flip process involves energetically higher-lying excited states as an

intermediate[15-19] (Fig. 1b). Since Equation (2) misses out such key intermediate information in the actual spin-flip process, recent calculations using the equilibrium geometries only provided qualitative justification of the experimental k_{RISC} for a handful of TADF molecules[20]. Herein, we explicitly compute singlet–triplet crossing seams to quantitatively predict k_{RISC} in vastly different structures of both literature and newly synthesized molecules. Rigorous comparison to experimental data reported over the last decade allows for a general understanding of the RISC kinetics governed by the singlet–triplet crossing seam involving a higher-lying excited state.

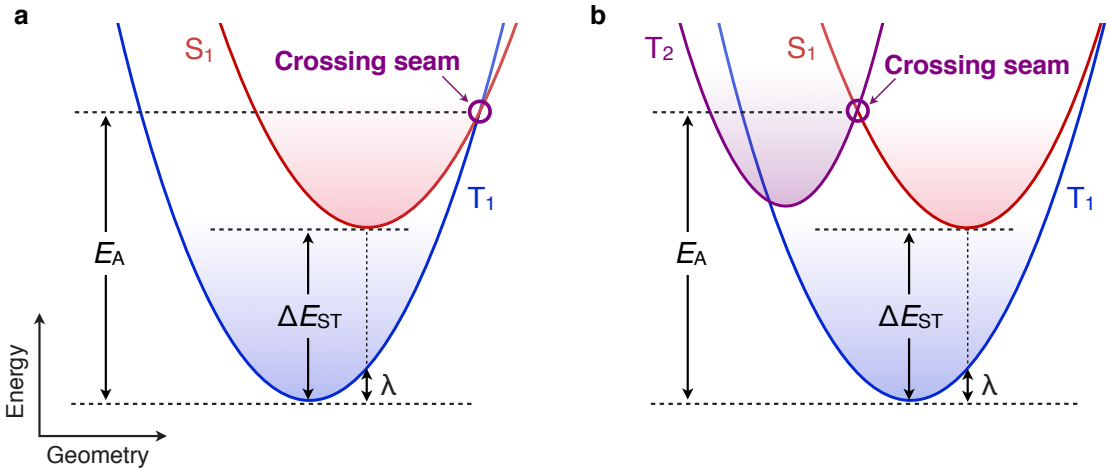

Fig. 1 | RISC from triplet to singlet excited states. a,b, Schematic potential energy surfaces of excited states depicting RISC via (a) their S_1–T_1 crossing seam and (b) S_1–T_2 crossing seam.

Results and discussion

To understand and predict the RISC kinetics, we first focus on twenty different TADF molecules reported in the literature (Fig. 2a). These molecules are characterized as donor–acceptor systems, whereby electron-rich donor units, aryl amines, are covalently bound to electron-deficient acceptor units, cyclic amines, aryl nitriles, ketones, boranes, sulfones, alkynes and phosphine oxides. We collected steady-state and transient photoluminescence data of these molecules from literature values, and estimated their k_{RISC} from differential rate equations for excited-state density (see Supplementary Information section 1 for details). The experimental k_{RISC} has a substantial variation of five orders of magnitude, from 10^2 to 10^7 s^{-1}.

Directly computing k_{RISC} from Equation (1) requires the minimum-energy seam of crossing (MESX), the energetically most accessible geometry on the singlet–triplet crossing seam hypersurface[21,22], as well as equilibrium excited-state geometries. To obtain MESXs for each molecule, we employed a constrained optimization algorithm using the gradient projection method[23], which minimizes the mean energy of singlet and triplet states $(E_S + E_T)/2$ while simultaneously fulfilling the crossing condition of the square energy difference $(E_S - E_T)^2 = 0$. E_S and E_T were calculated at the level of time-dependent density functional theory (TDDFT) within the Tamm–Dancoff approximation[24] (see Methods for details).

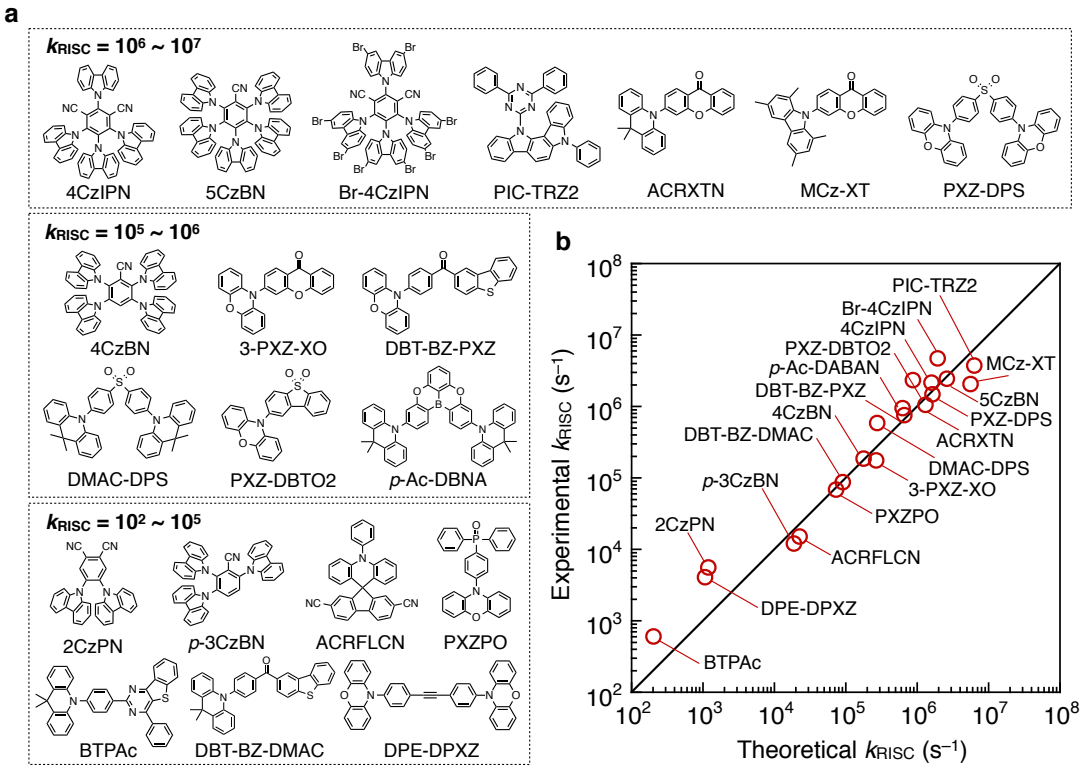

Fig. 2 | Twenty molecules examined in this study and their k_{RISC}. a, Molecular structures of the examined TADF materials categorized by k_{RISC}. **b**, Comparison of the experimental and theoretical k_{RISC}.

For the MESX geometries of the twenty molecules shown in Fig. 2a, the TDDFT predicts non-zero H_{SO} of 0.17–3.61 cm^{-1} with fairly small E_A of 0.11–0.32 eV, corresponding to k_{RISC} of 10^2–10^7 s^{-1} calculated using Equation (1) at T of 300 K. Fig. 2b compares the theoretical k_{RISC} to the experimental rates, demonstrating that the present model successfully reproduces the experimental rates. The mean

absolute logarithmic error (MALE) reaches only 0.23, whereas a larger MALE of 1.2, corresponding to an error of 1.2 orders of magnitude, is observed for using the parabolic approximation of Equation (2) (see Supplementary Fig. S1 for the errors for each molecule). These results thus demonstrate the importance of the explicit computation of singlet–triplet crossing seams in quantitatively predicting k_{RISC}.

Closer inspection on the data further reveals that the lowest singlet excited state (S_1) does not cross the lowest triplet state (T_1), but the higher-lying triplet states (T_2) at the obtained MESX geometries. Such feature well explains the larger errors for the parabolic approximation, which does not account for any higher-lying excited states. We attribute the uncrossed S_1 and T_1 to a non-zero exchange interaction between the singlet and triplet states, which leads to T_1 lying always below S_1 consistent with Hund's rule of maximum multiplicity if the two states have the same electronic configuration[25]. In accordance with El-Sayed's rule[26], a large change in the orbital angular momentum between S_1 and T_2 consisting of different electronic configurations induces effective H_{SO} and thus enable spin flipping via the MESX. These results are consistent with the RISC picture anticipated by the recent theoretical and experimental studies on ACRXTN[16] and 4CzIPN[19]. It must be stressed that the S_1–T_2 MESX is present in every molecule examined in this quantitative study despite their wide variety of excited-state electronic configurations, including intramolecular charge transfer (CT) states and locally excited (LE) states of π–π* and *n*–π* on either donor or acceptor units, illustrating the generality of RISC via S_1–T_2 crossing in organic donor–acceptor molecules.

To further validate the present RISC model of Equation (1), we computed k_{RISC} of novel brominated analogues of representative TADF materials ACRXTN and 3-PXZ-XO: 3-(2,7-dibromo-9,9-dimethylacridan-10-yl)xanthone (Br-ACRXTN) and 3-(3,7-dibromo-phenoxazin-10-yl)xanthone (Br-3-PXZ-XO) (Fig. 3a and b). Although heavy halogen atoms such as bromine are well known to induce large H_{SO} and thus facilitate ISC[27], the calculations predict that electrophilic bromination of ACRXTN counterintuitively decreases k_{RISC} from 1.3×10^6 s^{-1} to 7.1×10^5. In contrast, bromination of 3-PXZ-XO leads to over a hundredfold increase in k_{RISC} from 2.7×10^5 s^{-1} to 4.2×10^7 s^{-1}. Indeed, subsequent

synthesis and characterization confirm the predicted opposite trend; the bromination of ACRXTN and 3-PXZ-XO causes experimental k_{RISC} to decrease from 1.0×10^6 s^{-1} to 8.7×10^5 s^{-1} and to increase from 1.7×10^5 s^{-1} to 2.6×10^7 s^{-1}, respectively (see Supplementary Table S1 for details). To the best of our knowledge, k_{RISC} of over 10^7 s^{-1} for Br-3-PXZ-XO is higher than those ever reported for organic TADF materials[28]. Such high k_{RISC} reflects its fast transient photoluminescence decay with a delayed fluorescence lifetime of 490 ns (Fig. 3c), which is considerably shorter than typical values of several microseconds[29]. We also note that both brominated molecules exhibit similar blue shifts in their broad, unstructured CT emissions compared to the corresponding nonbrominated analogues (Fig. 3d), which is attributed to the electron-withdrawing effects of the bromine atoms on the donor units, destabilizing the CT states between the donor and acceptor units.

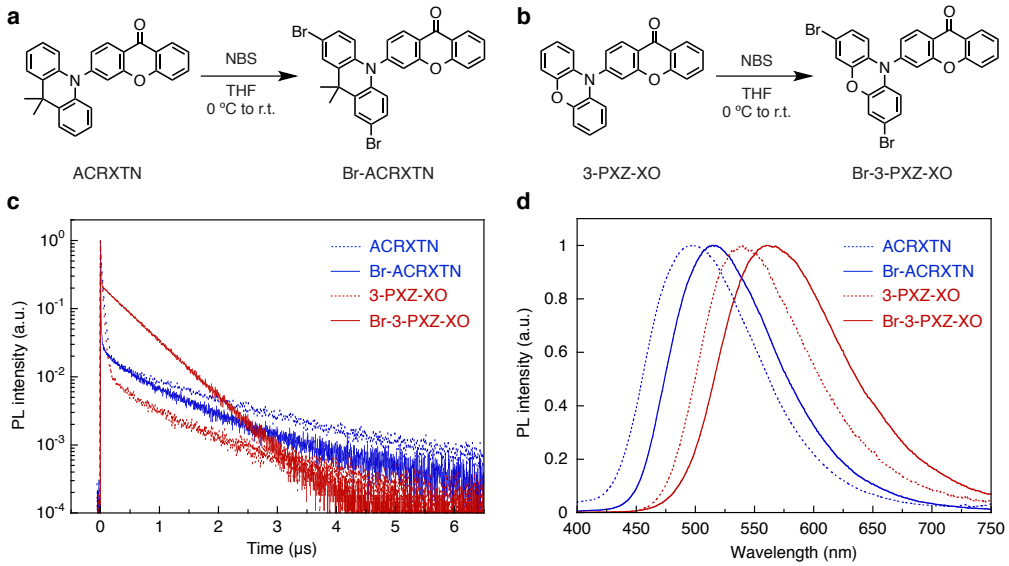

Fig. 3 | Synthesis and photoluminescence properties of novel molecules. a,**b**, Synthetic routes of Br-ACRXTN (**a**) and Br-3-PXZ-XO (**b**). **c**,**d**, Transient photoluminescence decays (**c**) and steady-state photoluminescence spectra (**d**) of ACRXTN, Br-ACRXTN, 3-PXZ-XO and Br-3-PXZ-XO in a solid-state host matrix 2,8-bis(diphenylphosphoryl)dibenzo[*b*,*d*]furan (PPF) at a doping concentration of 5wt%.

The notable retardation of k_{RISC} by bromination of ACRXTN is due to a decrease in H_{SO} from 0.88 cm^{-1} to 0.72 cm^{-1} at the S_1–T_2 MESX geometries. This counterintuitive substitution effects of bromine on H_{SO}

can be rationalized by two factors. First, the S_1–T_2 spin flipping in Br-ACRXTN is compensated by a smaller change in the orbital angular momentum than that in ACRXTN (Fig. 4a and b). This is due to an increase in the occupation of the CT state in T_2 from 28% to 57% upon bromination, which leads to both S_1 and T_2 characterized as similar CT states with small H_{SO} according to El-Sayed's rule. Additionally, the resulting change in the orbital angular momentum of Br-ACRXTN involves the *n* orbital of the carbonyl oxygen on the acceptor unit rather than bromine on the donor unit (Fig. 4b), suggesting its heavy atom effect plays a minor rule in determining H_{SO} between S_1 and T_2. In contrast, Br-3-PXZ-XO has a perceivable contribution of the bromine atoms to the orbital angular momentum change between S_1 of the CT state and T_2 of the LE π–π^* state on the donor unit (Fig. 4c and d). Such circumstances are indeed consistent with the heavy atom effect of bromine being responsible for an increase in H_{SO} from 1.2 cm^{-1} to 3.5 cm^{-1} and thus for the unprecedented high k_{RISC} over 10^7 s^{-1} in Br-3-PXZ-XO.

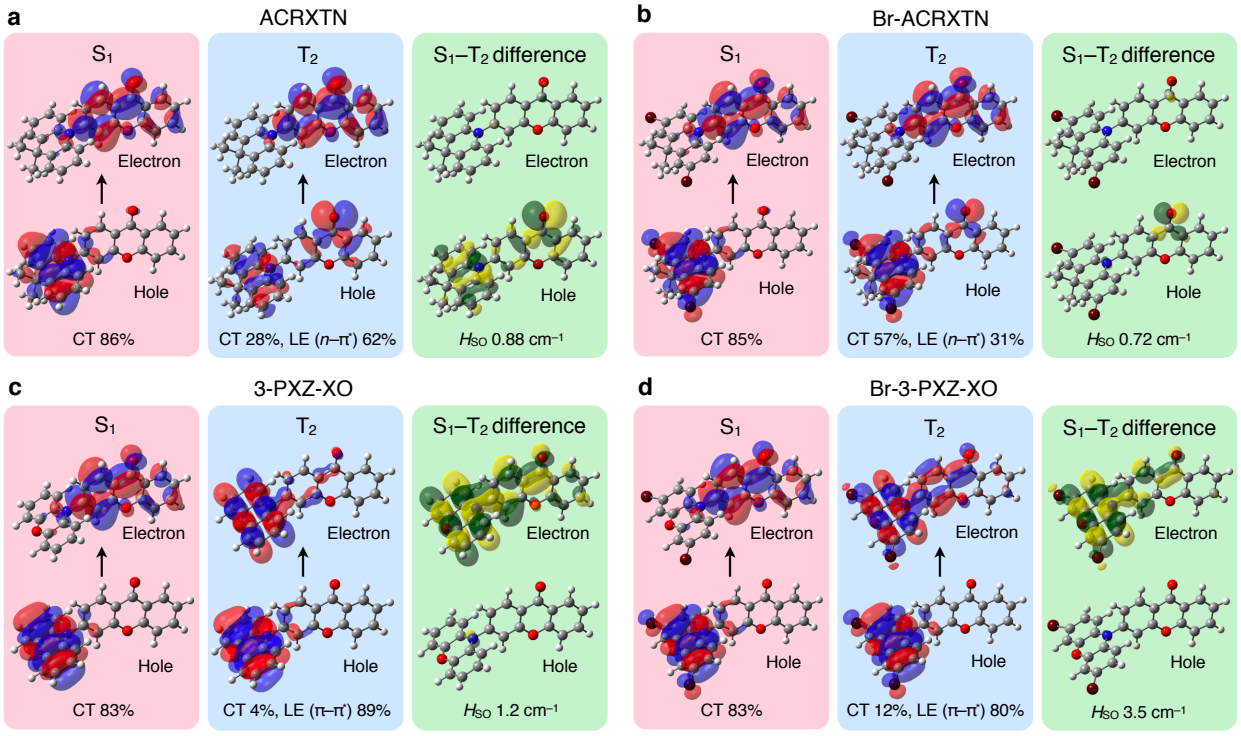

Fig. 4 | Electronic configurations of S_1–T_2 MESXs. a–d, Natural transition orbitals (NTOs) for the excited states of ACRXTN (**a**), Br-ACRXTN (**b**), 3-PXZ-XO (**c**) and Br-3-PXZ-XO(**d**) at S_1–T_2 MESX geometries. The differences in density between S_1 and T_2 NTOs are also shown.

Finally, we simulated the impact of varying H_{SO} and E_A on k_{RISC} (Fig. 5). While the existing organic TADF molecules exhibit k_{RISC} smaller than 10^8 s^{-1}, the theory predicts that even k_{RISC} of 10^9 s^{-1} corresponding to a time constant of 1.0 ns can be achieved with H_{SO} less than 10 cm^{-1}; for example, H_{SO} of 7.7 cm^{-1} for E_A of 0.10 eV and H_{SO} of 2.9 cm^{-1} for E_A of 0.05 eV at T of 300 K. These H_{SO} are an order of magnitude smaller than those of iridium-containing phosphors and could be achieved by exploiting heavy atom effects of nonmetals of periods 3 and 4[30,31]. However, we have shown that such heuristic approaches sometimes lead to retardation of H_{SO}, in part because of their more pronounced effects on the excited-state electronic configurations at S_1–T_2 MESX geometries. Thus, for new materials design, a priori computational screening is essential and the RISC model presented here allows for it.

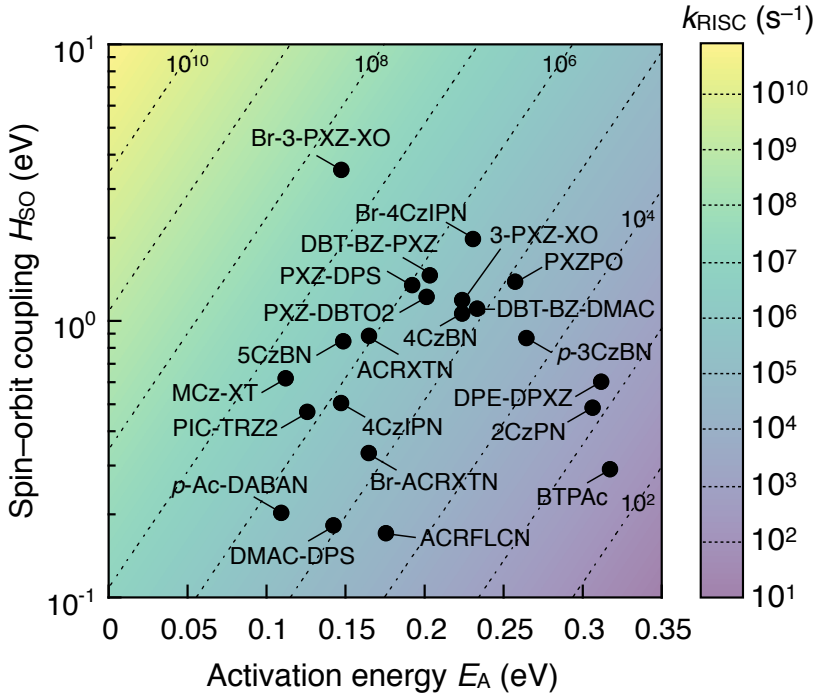

Fig. 5 | Overview of theoretical k_{RISC}. k_{RISC} as a function of H_{SO} and E_A with fixed λ of 0.10 eV and T of 300 K. H_{SO} and E_A of the examined molecules are also plotted.

In summary, we have presented a RISC kinetic model that successfully predicts experimental rates for a wide variety of organic TADF molecules. Our results suggest that explicitly computing singlet–triplet crossing seams leads to more reliable predictions than those by the conventional approach using the

Marcus parabolic approximation, because RISC in these molecules involves the higher-lying triplet excited states. The presented model is thus a viable tool for theory-driven materials discovery with a relevant exemplar exhibiting unprecedented high k_{RISC} of 2.6×10^7 s^{-1}. We envisage that a further computational screening of the vast chemical space will allow for discovery of novel materials exploiting the spin-flipping process for various photochemical applications.

Methods

Computation. Geometries of the singlet–triplet MESXs, where the square energy difference $(E_S - E_T)^2$ and the mean energy $(E_S + E_T)/2$ are minimized, were obtained by the gradient projection method[23] using a composed gradient vector $\boldsymbol{G}$ for the nuclear coordinates $\boldsymbol{Q}$:

$$\boldsymbol{G}(\boldsymbol{Q}) = 2\left(E_S(\boldsymbol{Q}) - E_T(\boldsymbol{Q})\right)\frac{\boldsymbol{v}}{|\boldsymbol{v}|} + \frac{1}{2}\left(\frac{\partial E_S(\boldsymbol{Q})}{\partial \boldsymbol{Q}} + \frac{\partial E_T(\boldsymbol{Q})}{\partial \boldsymbol{Q}}\right)\boldsymbol{P} \tag{3}$$

where

$$\boldsymbol{P} = 1 - \frac{\boldsymbol{v}\boldsymbol{v}^T}{|\boldsymbol{v}|^2} \tag{4}$$

In Equation (3), the first term contains the difference gradient vector $\boldsymbol{v}$ to minimize the energy difference. The second term is responsive for minimizing the mean energy, while the projection matrix $\boldsymbol{P}$ ensures the orthogonality between these two terms of the composed gradient vector. Excited-state energy and gradient were calculated using linear-response TDDFT with the LC-BLYP functional[32] and the 6-31+G(d) basis set within the Tamm–Dancoff approximation[24]. The range-separated parameters for the LC-BLYP functional were non-empirically optimized for each molecule to incorporate a reasonable amount of exact exchange[33,34]. The geometry optimization of MESXs was performed by the GRRM17 program[35], which refers to the energy and gradient calculated by the Gaussian 16 program[36]. H_{SO} was calculated perturbatively using the Breit–Pauli spin–orbit Hamiltonian with an effective charge approximation implemented in the PySOC program[37] interfaced to the Gaussian 16 program. E_A was calculated as the

electronic energy difference between the MESX and the equilibrium T_1. λ was calculated as the difference between the T_1 electronic energies at the equilibrium T_1 and S_1 geometries.

Chemical synthesis. The synthetic procedures and characterization data of novel compounds are detailed in Supplementary Information section 2.

Photoluminescence measurements. Steady-state photoluminescence spectra were acquired using a Fluoromax-4 spectrophotometer (HORIBA) with 370 nm photoexcitation from a Xe arc lamp. Transient photoluminescence decay measurements were performed under a flow of N_2 using a Fluorolog-3 fluorescence lifetime spectrometer (HORIBA) with a 370 nm LED excitation source. Absolute PL quantum yields were determined under a flow of N_2 using a C9920 integrating sphere system (Hamamatsu Photonics). The method of determining experimental k_{RISC} are detailed in Supplementary Information section 1.

Acknowledgements

This work was supported by JST PRESTO (Grant No. JPMJPR17N1 for N.A. and JPMJPR16N8 for Y.H.), Grant-in-Aid for JSPS KAKENHI Grant (No. JP20K15252 for N.A.) and JST-ERATO (Grant No. JPMJER1903 for S.M. and Y.H.). The computations were partially performed on the computer center of Kyoto University and the HOKUSAI system at RIKEN.

Author contributions

N.A. and Y.H. performed the theoretical calculations. N.A. synthesized the compounds and characterized the photoluminescence properties. S.M. and Y.J. supervised the project. All authors contributed to the discussion, writing and editing of the manuscript.

Competing interests

The authors declare no competing interests.

Additional information

The Supporting Information is available for determination of experimental k_{RISC}, synthesis and characterization.

References

1 Baldo, M. A. *et al.* Highly efficient phosphorescent emission from organic electroluminescent devices. *Nature* **395**, 151–154 (1998).

2 Rao, A. *et al.* The role of spin in the kinetic control of recombination in organic photovoltaics. *Nature* **500**, 435–439 (2013).

3 Einzinger, M. *et al.* Sensitization of silicon by singlet exciton fission in tetracene. *Nature* **571**, 90–94 (2019).

4 Theriot, J. C. *et al.* Organocatalyzed atom transfer radical polymerization driven by visible light. *Science* **352**, 1082–1086 (2016).

5 Lim, C.-H. *et al.* Intramolecular charge transfer and ion pairing in *N,N*-diaryl dihydrophenazine photoredox catalysts for efficient organocatalyzed atom transfer radical polymerization. *J. Am. Chem. Soc.* **139**, 348–355 (2017).

6 Singh, V. K. *et al.* Highly efficient organic photocatalysts discovered via a computer-aided-design strategy for visible-light-driven atom transfer radical polymerization. *Nat. Catal.* **1**, 794–804 (2018).

7 Henderson, B. W. & Dougherty, T. J. How does photodynamic therapy work? *Photochem. Photobiol.* **55**, 145–157 (1992).

8 Xiong, X. *et al.* Thermally activated delayed fluorescence of fluorescein derivative for time-resolved and confocal fluorescence imaging. *J. Am. Chem. Soc.* **136**, 9590–9597 (2014).

9 Zhen, X. *et al.* Ultralong phosphorescence of water-soluble organic nanoparticles for in vivo afterglow imaging. *Adv. Mater.* **29**, 1606665 (2017).

10 Uoyama, H., Goushi, K., Shizu, K., Nomura, H. & Adachi, C. Highly efficient organic light-emitting diodes from delayed fluorescence. *Nature* **492**, 234–238 (2012).

11 Marcus, R. A. Electron transfer reactions in chemistry: theory and experiment (Nobel lecture). *Angew. Chem. Int. Ed.* **32**, 1111–1121 (1993).

12 Samanta, P. K., Kim, D., Coropceanu, V. & Brédas, J.-L. Up-conversion intersystem crossing rates in organic emitters for thermally activated delayed fluorescence: impact of the nature of singlet vs triplet excited states. *J. Am. Chem. Soc.* **139**, 4042–4051 (2017).

13 Olivier, Y. *et al.* Nature of the singlet and triplet excitations mediating thermally activated delayed fluorescence. *Phys. Rev. Mater.* **1**, 075602 (2017).

14 Olivier, Y., Sancho-Garcia, J.-C., Muccioli, L., D'Avino, G. & Beljonne, D. Computational Design of Thermally Activated Delayed Fluorescence Materials: The Challenges Ahead. *J. Phys. Chem. Lett.* **9**, 6149–6163 (2018).

15 Chen, X.-K., Zhang, S.-F., Fan, J.-X. & Ren, A.-M. Nature of highly efficient thermally activated delayed fluorescence in organic light-emitting diode emitters: nonadiabatic effect between excited states. *J. Phys. Chem. C* **119**, 9728–9733 (2015).

16 Marian, C. M. Mechanism of the triplet-to-singlet upconversion in the assistant dopant ACRXTN. *J. Phys. Chem. C* **120**, 3715–3721 (2016).

17 Gibson, J., Monkman, A. P. & Penfold, T. J. The importance of vibronic coupling for efficient reverse intersystem crossing in thermally activated delayed fluorescence molecules. *ChemPhysChem* **17**, 2956–2961 (2016).

18 Etherington, M. K., Gibson, J., Higginbotham, H. F., Penfold, T. J. & Monkman, A. P. Revealing the spin–vibronic coupling mechanism of thermally activated delayed fluorescence. *Nat. Commun.* **7**, 13680 (2016).

19 Noda, H. *et al.* Critical role of intermediate electronic states for spin-flip processes in charge-transfer-type organic molecules with multiple donors and acceptors. *Nat. Mater.* **18**, 1084–1090 (2019).

20 Park, I. S., Matsuo, K., Aizawa, N. & Yasuda, T. High-Performance Dibenzoheteraborin-Based Thermally Activated Delayed Fluorescence Emitters: Molecular Architectonics for Concurrently Achieving Narrowband Emission and Efficient Triplet–Singlet Spin Conversion. *Adv. Funct. Mater.* **28**, 1802031 (2018).

21 Koga, N. & Morokuma, K. Determination of the lowest energy point on the crossing seam between two potential surfaces using the energy gradient. *Chem. Phys. Lett.* **119**, 371–374 (1985).

22 Harvey, J. N. Understanding the kinetics of spin-forbidden chemical reactions. *Phys. Chem. Chem. Phys.* **9**, 331–343 (2007).

23 Bearpark, M. J., Robb, M. A. & Schlegel, H. B. A direct method for the location of the lowest energy point on a potential surface crossing. *Chem. Phys. Lett.* **223**, 269–274 (1994).

24 Hirata, S. & Head-Gordon, M. Time-dependent density functional theory within the Tamm–Dancoff approximation. *Chem. Phys. Lett.* **314**, 291–299 (1999).

25 Slater, J. C. The theory of complex spectra. *Phys. Rev.* **34**, 1293–1322 (1929).

26 El-Sayed, M. Spin–Orbit Coupling and the Radiationless Processes in Nitrogen Heterocyclics. *J. Chem. Phys.* **38**, 2834–2838 (1963).

27 Turro, N. J. *Modern Molecular Photochemistry* (University Science Books, 1991).

28 Wada, Y., Nakagawa, H., Matsumoto, S., Wakisaka, Y. & Kaji, H. Molecular Design Realizing Very Fast Reverse Intersystem Crossing in Purely Organic Emitter. *ChemRxiv*, https://doi.org/10.26434/chemrxiv.9745289 (2019).

29 Liu, Y., Li, C., Ren, Z., Yan, S. & Bryce, M. R. All-organic thermally activated delayed fluorescence materials for organic light-emitting diodes. *Nat. Rev. Mater.* **3**, 18020 (2018).

30 de Sa Pereira, D. *et al.* The effect of a heavy atom on the radiative pathways of an emitter with dual conformation, thermally-activated delayed fluorescence and room temperature phosphorescence. *J. Mater. Chem. C* **7**, 10481–10490 (2019).

31 Drummond, B. H. *et al.* Selenium Substitution Enhances Reverse Intersystem Crossing in a Delayed Fluorescence Emitter. *J. Phys. Chem. C* **124**, 6364–6370 (2020).

32 Iikura, H., Tsuneda, T., Yanai, T. & Hirao, K. A long-range correction scheme for generalized-gradient-approximation exchange functionals. *J. Chem. Phys.* **115**, 3540–3544 (2001).

33 Baer, R., Livshits, E. & Salzner, U. Tuned range-separated hybrids in density functional theory. *Annu. Rev. Phys. Chem.* **61**, 85–109 (2010).

34 Sun, H., Zhong, C. & Bredas, J.-L. Reliable prediction with tuned range-separated functionals of the singlet–triplet gap in organic emitters for thermally activated delayed fluorescence. *J. Chem. Theory Comput.* **11**, 3851–3858 (2015).

35 Maeda, S. *et al.* Implementation and performance of the artificial force induced reaction method in the GRRM17 program. *J. Comput. Chem.* **39**, 233–251 (2018).

36 Frisch, M. J. *et al.* Gaussian 16 Rev. C.01. (Wallingford, CT).

37 Gao, X. *et al.* Evaluation of spin-orbit couplings with linear-response time-dependent density functional methods. *J. Chem. Theory Comput.* **13**, 515–524 (2017).